Applied Thermal Engineering 143 (2018) 1079–1084

Contents lists available at ScienceDirect

Applied Thermal Engineering

journal homepage: www.elsevier.com/locate/apthermeng

Research Paper

Low-cost high-efficiency solar steam generator by combining thin film evaporation and heat localization: Both experimental and theoretical study

Guilong Peng[a,b,1], Hongru Ding[a,b,1], Swellam Wafa Sharshir[a,b,c], Xiaojia Li[a,b], Hanchen Liu[a,b], Dengke Ma[a,b], Lirong Wu[a,b], Jianfeng Zang[d,e], Huan Liu[d], Wei Yu[f], Huaqing Xie[f], Nuo Yang[a,b,*]

[a] State Key Laboratory of Coal Combustion, Huazhong University of Science and Technology, Wuhan 430074, China
[b] Nano Interface Center for Energy (NICE), School of Energy and Power Engineering, Huazhong University of Science and Technology, Wuhan 430074, China
[c] Mechanical Engineering Department, Faculty of Engineering, Kafrelsheikh University, Kafrelsheikh, Egypt
[d] School of Optical and Electronic Information, Huazhong University of Science and Technology, Wuhan 430074, China
[e] Innovation Institute Huazhong University of Science and Technology, Wuhan 430074, China
[f] School of Environment and Materials Engineering, College of Engineering, Shanghai Polytechnic University, Shanghai 201209, China

ARTICLE INFO

Keywords:
Steam generation
Solar energy
Graphite micro/nano particles
Thin-film evaporation

ABSTRACT

Generating water steam is a significant process for many fields. By combining heat localization and thin-film evaporation, a low-cost high-efficiency solar steam generator is proposed here. The measurements show that the energy efficiency is 78% at 1 kW/m^2. Meanwhile, the experimental results agree well with our theoretical prediction based on thin-film evaporation theory. Besides, the dependence of efficiency on particle concentration and size are discussed. It's found that the performance of the generator has a weak correlation to a few different particles (graphite, graphene, MoS_2, and carbon nanotubes). This work offers a new in-depth understanding of high-efficiency solar steam generation and shows an example of using nanotechnology in practical application by a cheap and simple way.

1. Introduction

Solar energy is abundant, renewable and eco-friendly, hence high efficiency solar energy harvesting technology becomes one of the most popular research topic. Solar steam generation technology, as one of the ways to utilize solar energy, has a lot of applications such as desalination [1–3], power generation [4–6], water purification [7], oil recovery [8,9] and so on.

During the past decades, many works have been devoted to harvesting the solar energy for steam generation, for example, designing a high efficiency solar still [10–21]. Various types of solar still like the stepped solar still [18] and wick type solar still [19,20] have been developed. However, the energy efficiency of those traditional solar stills are normally below 50% due to the large heat loss. Recently, a new effective method named heat localization was proposed to enhance the evaporation efficiency [22–29]. It's based on the thermal insulation between the evaporation region and the bulk water. The evaporation efficiency reaches up to 67% under 1 kW/m^2 by using a double layer structure, which is constructed by expanded graphite and carbon foam [23]. And the efficiency increases to 80% when the double layer structure is constructed by graphene oxide and polystyrene [24]. By using an aluminum nanoparticles coated nanoporous Al_2O_3 film, the efficiency will be 91% under 6 kW/m^2 insolation [29]. However, due to the complex design, the material cost in these researches is too high for large-scale applications.

Another promising strategy to enhance evaporation is utilizing thin-film evaporation [30–35]. When liquid wets a solid wall, the extended meniscuses are typically divided into three regions: adsorbed region (I), thin-film region (II) and intrinsic meniscus region (III). The strongest evaporation happens at the surface of region II due to the very low thermal resistance across the liquid film. Therefore, the heat loss to the surrounding water is very low, hence the high energy efficiency. Micro [31] or nano [32] scale surface modifications and adding nanoparticles [33] or microparticles [34] in water are ways to increase the thin film region for higher energy efficiency. Besides, the efficiency can also be increased by improving the wettability of the solid wall [35].

In this paper, we combined thin film evaporation with heat localization, and proposed a low-cost high-efficiency wick type steam generator. We first studied the evaporation of bare water and steam generator with wick material to show the effect of heat localization. Then,

* Corresponding author at: State Key Laboratory of Coal Combustion, Huazhong University of Science and Technology, Wuhan 430074, China.
E-mail address: nuo@hust.edu.cn (N. Yang).
[1] Guilong Peng and Hongru Ding contribute equally on this work.

https://doi.org/10.1016/j.applthermaleng.2018.08.004
Received 2 May 2018; Received in revised form 26 July 2018; Accepted 2 August 2018
Available online 07 August 2018
1359-4311/

the effect of thin-film evaporation was studied quantitatively: we measured the evaporation rate of water from wick material with and without micro/nano particles. We also investigated the optimal concentration and size effect of particles, followed by the theoretical analysis of thin-film evaporation. In addition, the surfactant was used to further improve the efficiency. This paper shows an example of using nanotechnology in practical application by a cheap and simple way.

2. Work principle and experiment setup

The schematic diagram of evaporation is shown in Fig. 1a. Water is transported from the bottom to the top of the structure via the side wick by capillary action, then heated by solar energy and evaporates. The optical microscopic image of wetted wick is shown in Fig. 1b. The adiabatic foam can prevent the heat transfer between the top surface of the wick and the bulk water. Compared with the porous foam [23,29], which has relative high thermal conductivity when fully filled with water, the waterproof type adiabatic material has better performance. The schematic diagram of the measuring setup is illustrated in Fig. S1 at Supplemental Information.

Supplementary data associated with this article can be found, in the online version, at https://doi.org/10.1016/j.applthermaleng.2018.08.004.

To further increase the evaporation rate, graphite micro/nano particles were sprinkled and smeared uniformly on the evaporation surface to create more thin-film region. The flake graphite particles are inherently hydrophilic (water contact angle $< 90°$) [36–38]. Graphite particles that exposed to the air will be more hydrophilic than the pristine particles, due to the absorbed impurities on particles' surface [36]. The process of applying particles is shown in the Supplementary Video 1 and Video 2. The adhesion between graphite particles and linen cloth is strong enough for daily use. Apart from increasing thin-film region, the high solar absorption, stability and thermal conductivity of graphite particles [17,39–43] can also improve the performance of the generator. The optical microscopic image of wetted wick with graphite particles on it is presented in Fig. 1c. It should be noted that the particles can be recycled easily by filtering as shown in Fig. S2. The scanning electron microscope (SEM) images of graphite particles are shown in Fig. S3. The retail price of graphite particles is around $10/kg, which is very cheap compared to most nano-materials.

Meanwhile, compared with porous materials in most works, our design are more anti-fouling, due to the small pores in porous materials of other works are easily blocked by pollutant in water. Therefore, porous materials need to be cleaned or changed periodically. However, there is no nano/micro pore in our system and the blocking can be avoid, which further decreases the maintain cost. It is also worth noting that our system is more mechanically flexible than other nanoporous material based system. That is, we can design the evaporation surface in any shape due to the mechanical flexibility of wick material.

The schematic diagram of the microscopic structure on the evaporation surface is shown in Fig. 1d. The particles on the fiber form a porous structure whose surface is filled with meniscuses. As illustrated in the inset of Fig. 1d, meniscus is constructed by three regions: (I) adsorbed or non-evaporation region, where water is adsorbed on the graphite due to the high disjoining pressure; (II) thin-film or transition region where effects of long-range molecular forces are felt; (III) intrinsic meniscus region, where the thickness of water layer increases very fast [44]. In the adsorbed region, water sticks to the graphite tightly and no mass/heat transfer occurs. Whereas in the thin-film region, the disjoin pressure is weak, while the thickness of water layer is still thin enough to assure a low thermal resistance. Therefore, the most heat current runs through the thin-film region, hence the fast evaporation and low heat loss.

Here, the black linen cloth and expanded polyethylene (EPE) were chosen as the wick material and adiabatic material, respectively (shown in Fig. S4). However, some other low-cost daily materials can also be chosen as the wick material, such as cotton, tissue, paper and so on, as long as the capillary action is strong enough to compensate the evaporation loss. The capillary action ability of the wick material can be described by the rate of moisture regain, which is 12.5% for linen [45] and 8.5% for cotton [46]. The retail price of the linen cloth is around $\$5/m^2$. On the other side, the adiabatic material should meet the demand of waterproof and floating on the water. The EPE is low-cost (retail price, $\sim\$1/m^2$), recyclable, anticorrosion and nontoxic. It's safer compared with other common adiabatic materials, like rubber insulation cotton and expanded polystyrene. The characteristics of the linen and EPE are listed in Table S1.

3. Results and discussion

Three cases are investigated to study the effects of the wick mate-

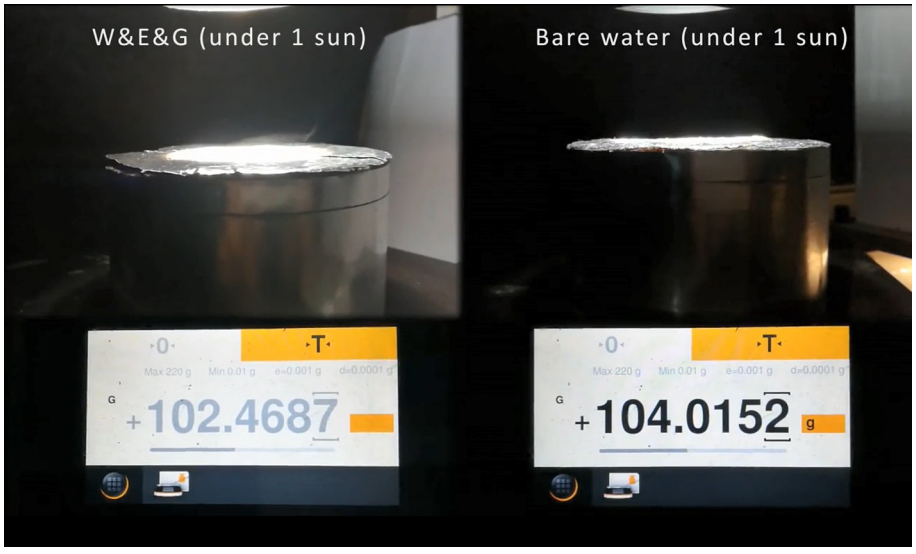

Video 2.

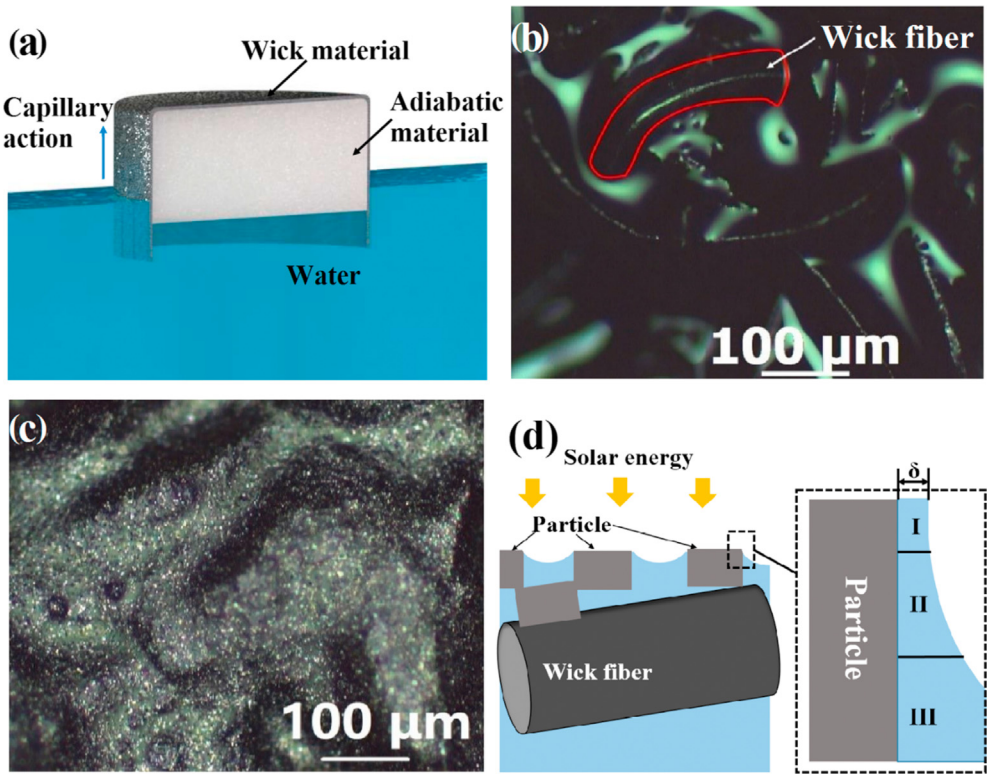

Fig. 1. (a) Schematic diagram of evaporation. Particles are used for a better heat transferring to surface water, while the insulation material is used for preventing the heat transfer between surface water and bulk water. (b) The optical microscopic image of the wetted wick material. (c) The optical microscopic image of the wetted wick material covered by graphite particles. The average size and thickness of the particles are around 1.3 μm and 100 nm, respectively. (d) Schematic diagram of the microscopic structure on the evaporation surface. The inset shows the meniscus near the particle. Region (I)-(III) are adsorbed region, thin film region and intrinsic meniscus region, respectively. The fastest evaporation happens at thin-film region.

rial, EPE and graphite particles on the evaporation rate. The first one is using bare water only. The bare water in a cup is around 60 g in mass and 5 cm in depth. As shown in Fig. 2a, the evaporation rate of bare water is very low, and the accumulated mass reduction due to the evaporation is less than 0.15 kg/m^2 in 30 min. The natural evaporation rate is measured at around 0.11 kg/(m^2·h) at room environment (temperature 24 °C and relative humidity 40%). All the values shown here has subtracted the natural evaporation rate already.

The second one is using both wick material and EPE (W&E) to enhance evaporation. The mass reduction of water reaches to 0.37 kg/m^2 in half an hour, which is 2.5 times that of bare water according to Fig. 2a. When the evaporation reaches stable state (after 800 s), the hourly evaporation rate is 0.76 kg/(m^2·h).

The third one is using wick material, EPE and graphite particles (W&E&G). The results show that graphite particles can further enhance evaporation. Mass reduction is 0.52 kg/m^2 in 30 min and hourly

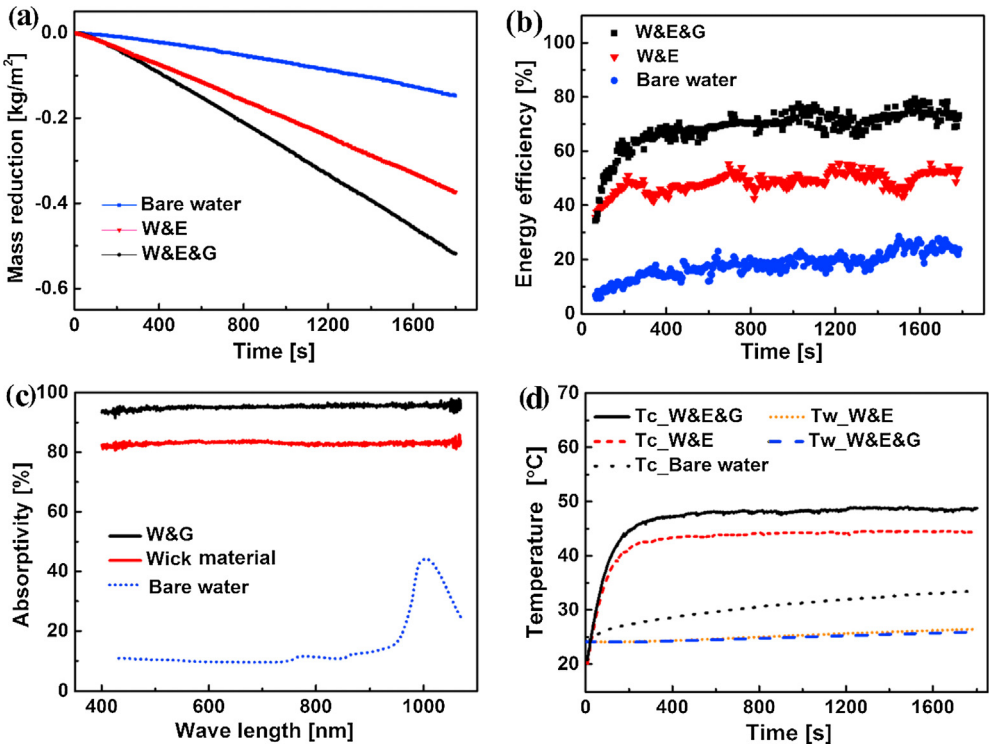

Fig. 2. (a) The mass reduction due to evaporation versus time of three different systems: bare water, with wick and EPE (W&E), and with wick, EPE and graphite particles (W&E&G). The concentration for graphite is 60 g/m^2, the lateral size of particles is around 1.3 μm (10,000 mesh). (b) The instantaneous energy efficiency of three different systems. (c) The absorptivity of bare water, the wetted wick material, the wetted wick material with graphite particles (W&G). (d) The temperature of different systems. T_c is the temperature at the center of the evporation surface. T_w is the temperature of water 1 cm below EPE or the surface of bare water. The surface temperature of water is measured by placing a thermocouple on the evaporation surface, where the same method is used in Ref. [23].

evaporation rate after 800 s is 1.06 kg/(m^2·h), which is 40% higher than that of W&E.

The relationship between the evaporation rate and energy efficiency is described as [29]:

$$\eta = \frac{\Delta m \cdot h_{LV}}{Q} \quad (1)$$

where η is the energy efficiency, Δm is the evaporation rate, h_{LV} is the total enthalpy of phase change, containing latent heat and sensible heat, Q is the incident solar energy.

The instantaneous energy efficiency of evaporation is shown in Fig. 2b. As we can see, the evaporation efficiency of bare water is continuously increasing during the measurement, which reaches to around 28% after half an hour. On the contrary, for W&E and W&E&G, it is faster to converge and get the maximum efficiency. The energy efficiencies reach 52% and 73% for W&E and W&E&G, respectively. Obviously, the utilization of wick, EPE and graphite particles is very effective for enhancing the energy efficiency.

There are three main factors, the heat localization, the absorptivity and the micro/nano particles, responsible for the enhancement which will be analyzed in the following.

Firstly, the temperatures are measured by T-type thermocouples to show the performance of heat localization. The surface temperature of bare water keeps increasing and reaches to 34 °C after 30 min as shown in Fig. 2c. There is a considerable proportion of the absorbed energy is used for increasing the bulk water temperature instead of evaporation, which reduces the energy efficiency. On the other hand, the surface temperatures of W&E and W&E&G can reach up to a stable state at 44.5 °C and 48.5 °C, respectively. Due to the heat localization by adiabatic material, only the water in the thin wick material is heated and the other water below the adiabatic material will not obtain heat. That is, almost all the heat is localized at the thin wick material, which results in the high surface temperature and fast evaporation. The design of our system has a higher heat localization effect than that of porous structure [23,28,29].

Secondly, to understand the high performance of evaporation by wick material, the absorptivity of different materials is measured firstly. As shown in Fig. 2c, the absorptivity of water is around 10% at 1 cm in thickness. The absorptivity reaches up to 83% for wetted wick material, and can be further increased to 95% when the graphite particles are added on the wick material. The higher absorptivity results in higher energy efficiency. However, energy efficiency increases by 21% after adding the graphite particles, which is much higher than the increase on absorptivity (12%). The possible reason is that the heat transfer is improved and the evaporation from thin-film region is increased by the graphite particles, which have high thermal conductivity and large specific surface area.

In the last, we investigate the effect of the concentration of micro/nano particles to obtain a better performance of our system. Interestingly, as seen in Fig. 3a, there is a steep increase in the efficiency (~17%) when the concentration increases from 0 to 20 g/m^2. It implies that the graphite particles play a very important role in solar evaporation. The optimal concentration is found at 60 g/m^2. Then the efficiency will decrease slightly for higher concentration. The absorptivity of different concentration is the same as shown in Fig. S5. The increase may be due to the sufficient thin-film region when increasing concentration. At high concentration (> 60 g/m^2), the reduction of efficiency may come from the impeded water supply and the decreased thin-film region on the surface by thick graphite mud layer, due to that the water transportation path is blocked by the severely aggregated graphite particles.

To decrease aggregation and improve the wettability of particles, which increase the thin-film region [23,35], we applied anionic surfactant on particles. The surfactant is dropped and smeared on the particles. Fig. 3c shows that the maximum efficiency reaches up to 78% when the concentration of particle is 60 g/m^2, which is 5% higher than that of without surfactant. The optimal concentration of surfactant is around 0.5–1 g/m^2. The efficiency begins to decrease when the concentration of surfactant is higher, because the water surface is almost covered by surfactant, which impedes the evaporation [47].

Another important factor, particle size, is also considered here. As shown in Fig. 3b, the evaporation rate is inversely proportional to the

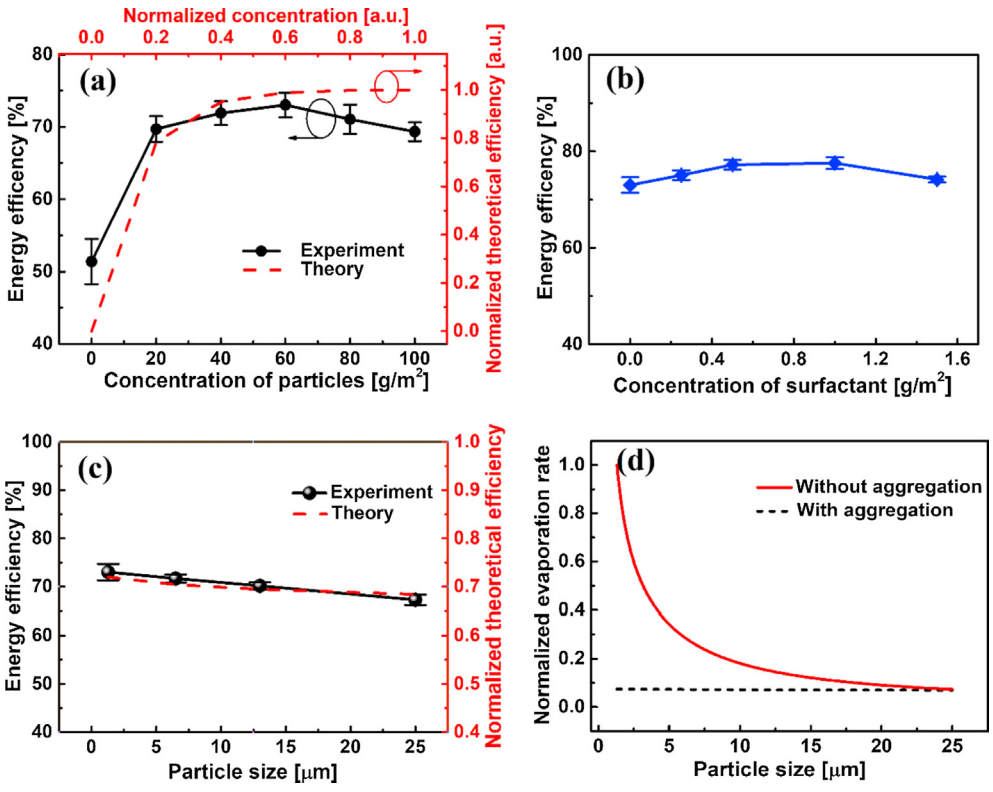

Fig. 3. (a) The energy efficiency for different graphite concentration on wick material. The theoretical predictions are based on the thin-film theory. (b) The effect of anionic surfactant (sodium laurylsulfonate) on the efficiency, where the concentration of graphite particles is 60 g/m^2. (c) The energy efficiency for different graphite size on wick material. (d) The theoretical prediction of evaporation rate with/without considering the aggregation.

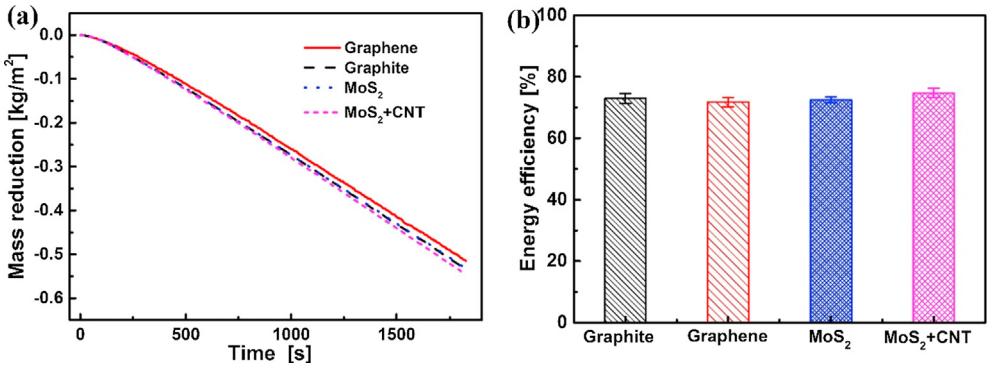

Fig. 4. (a) The mass reduction of water for different materials. (b) The energy efficiency of different materials. The thickness of the graphite particles, multilayer graphene and MoS_2 are around 100 nm, 5 nm and 10 nm, respectively. The lateral size of the graphite particles, multilayer graphene and MoS_2 are around 1 μm, 50 μm and 10 μm, respectively. The diameter and length of the multi-walled CNT are about 50 nm and 2 μm, respectively. The mass percentage of the CNT in the mixture is 50%.

particle size, due to less particle-water interface and thin-film regions exist for larger particle size. When the size increases to 25 μm, the efficiency decreases by around 6% compared with that of 1.3 μm. The observed size effect is consistent with the theoretical analysis of thin-film evaporation as follows.

The measurement results will be compared to the prediction of thin-film evaporation theory. The mass reduction of thin-film evaporation per unite area is given by [48]:

$$\Delta m_t(d) = \frac{k}{\delta(d)\cdot h_{LV}}(T_{sl}-T_{lv}) \tag{2}$$

where k is the thermal conductivity of water film, h_{LV} is the enthalpy of vaporization. Both k and h_{LV} are constants [49]. $\delta(d)$ is the thickness of thin film (details in SI), T_{sl} is the temperature of graphite-water interface and T_{lv} is the temperature of water-vapor interface. Here, $T_{sl}-T_{lv}$ is assumed to be independent on particle size. The gross mass reduction of thin-film evaporation is given by:

$$\Delta M_t = A\cdot\Delta m_t \tag{3}$$

$$A \propto \frac{1}{d\cdot\alpha(d)} \tag{4}$$

where A is the area of the thin-film region; d is the characteristic length of graphite particle; $\alpha(d)$ is the sticking coefficient, i.e. the probability that two graphite particles aggregate [50]. A large $\alpha(d)$ indicates that the particles are sticking more tightly, which decreases the thin-film region because of less contact area between water and particles. Here we use an inverse proportion function to describe the sticking coefficient $\alpha(d)$ (details in SI), due to the smaller particles aggregate more severe [51].

The evaporation in the intrinsic region can be defined as:

$$\Delta M_i = \beta\Delta M_t \tag{5}$$

where β is the ratio between intrinsic evaporation and thin-film evaporation, β is regard as constant at 0.25 in our system according to Ranjan et al. [52]. Therefore, the total evaporation rate is described as:

$$\Delta M \propto \frac{1}{d\cdot\delta(d)\cdot\alpha(d)} \tag{6}$$

The theoretical efficiency for different particle concentrations and sizes is shown in Fig. 3a and Fig. 3c (orange line), respectively. To calculate the theoretical efficiency, the trend of aggregation for different concentration is obtained from Ref. [53]. As we can see, the theoretical and experimental results agree well with each other, which means that the system performance can be predicted very well by the thin-film evaporation theory. Meanwhile, as shown in Fig. 3d, when $\alpha(d)$ is neglected, the ideal normalized thin-film evaporation rate for different particle size shows a great difference. On the contrary, the difference is very small when particles aggregate. It indicates that improving the dispersion of particles is an effective way to further enhance the evaporation rate.

In addition, we measured the water evaporation rate when using several different materials, including the multilayer graphene, multilayer molybdenum disulfide (MoS_2) and the mixture of MoS_2 and carbon nanotube (CNT). The results are shown in Fig. 4. It shows that the evaporation rate and the energy efficiency are very similar and have a weak correlation to the material of particles. Given the material cost, the graphite particles are the most practical candidate for solar vapor generation. The results in Fig. 4 also indicate that the proposed generator has a high freedom in choosing particles, which is favorable in real applications.

4. Conclusion

In conclusion, the energy efficiency of the steam generator reaches up to 78% when using wick, expanded polyethylene, graphite particles and surfactant. Meanwhile, the material cost of the proposed generator is significantly lower (< $\$7/m^2$) compared with the most of the high efficiency nanotechnologies. The efficiencies are 52% and 73% for evaporation from wick with and without graphite particles, respectively. The graphite particles enhance the efficiency dramatically, due to the better solar absorption, heat localization and heat transfer. The results also indicate that the thin-film evaporation resulted from graphite particles can enhance the efficiency by 9%. The optimal concentration of graphite particles is 60 g/m^2 for the given condition. It's also found that the smaller the particle size, the higher the efficiency, due to more thin-film regions can be created by small particles. Meanwhile, the theoretical analysis implies that the energy efficiency can be further increased if the particles are better dispersed. In addition, the water evaporation rate shows a weak correlation to a few different particles (graphite, graphene, MoS_2, and carbon nanotubes), which indicates that the proposed generator has a high freedom in choosing particles.

The proposed low-cost high-efficiency steam generator may have broad applications, such as desalination and power generation. Also, the theoretical analysis helps to understand the interior reasons of high-efficiency steam generation and may provide the guideline of steam generator design.

Conflicts of interest

There is no conflict of interest to declare.

Acknowledgement

N.Y. was sponsored by National Natural Science Foundation of China (No. 51576076 and No. 51711540031), Hubei Provincial Natural Science Foundation of China (2017CFA046) and Fundamental Research Funds for the Central Universities (2016YXZD006). The authors thank the National Supercomputing Center in Tianjin (NSCC-TJ) and China Scientific Computing Grid (ScGrid) for providing assistance in computations.

References

[1] S.W. Sharshir, G. Peng, N. Yang, M.A. Eltawil, M.K.A. Ali, A.E. Kabeel, A hybrid desalination system using humidification-dehumidification and solar stills integrated with evacuated solar water heater, Energy Convers. Manage. 124 (2016) 287–296.

[2] M.R. Karimi Estahbanati, A. Ahsan, M. Feilizadeh, K. Jafarpur, S.-S. Ashrafmansouri, M. Feilizadeh, Theoretical and experimental investigation on internal reflectors in a single-slope solar still, Appl. Energy 165 (2016) 537–547.

[3] A.E. Kabeel, Z.M. Omara, F.A. Essa, Improving the performance of solar still by using nanofluids and providing vacuum, Energy Convers. Manage. 86 (2014) 268–274.

[4] T. Pirasaci, D.Y. Goswami, Influence of design on performance of a latent heat storage system for a direct steam generation power plant, Appl. Energy 162 (2016) 644–652.

[5] O. Behar, A. Khellaf, K. Mohammedi, A review of studies on central receiver solar thermal power plants, Renew. Sust. Energy Rev. 23 (2013) 12–39.

[6] M. Romero, A. Steinfeld, Concentrating solar thermal power and thermochemical fuels, Energy Environ. Sci. 5 (2012) 9234–9245.

[7] M.A. Shannon, P.W. Bohn, M. Elimelech, J.G. Georgiadis, B.J. Marinas, A.M. Mayes, Science and technology for water purification in the coming decades, Nature 452 (2008) 301–310.

[8] M. Absi Halabi, A. Al-Qattan, A. Al-Otaibi, Application of solar energy in the oil industry—Current status and future prospects, Renew. Sust. Energy Rev. 43 (2015) 296–314.

[9] J. Sandler, G. Fowler, K. Cheng, A.R. Kovscek, Solar-generated steam for oil recovery: Reservoir simulation, economic analysis, and life cycle assessment, Energy Convers. Manage. 77 (2014) 721–732.

[10] A.S. Abdullah, Improving the performance of stepped solar still, Desalination 319 (2013) 60–65.

[11] B.A.K. Abu-Hijleh, Enhanced solar still performance using water film cooling of the glass cover, Desalination 107 (1996) 235–244.

[12] I. Al-Hayeka, O.O. Badran, The effect of using different designs of solar stills on water distillation, Desalination 169 (2004) 121–127.

[13] O. Ansari, M. Asbik, A. Bah, A. Arbaoui, A. Khmou, Desalination of the brackish water using a passive solar still with a heat energy storage system, Desalination 324 (2013) 10–20.

[14] M. Dashtban, F.F. Tabrizi, Thermal analysis of a weir-type cascade solar still integrated with PCM storage, Desalination 279 (2011) 415–422.

[15] A.J.N. Khalifa, A.S. Al-Jubouri, M.K. Abed, An experimental study on modified simple solar stills, Energy Convers. Manage. 40 (1999) 1835–1847.

[16] S. Nijmeh, S. Odeh, B. Akash, Experimental and theoretical study of a single-basin solar sill in Jordan, Int. Commun. Heat Mass 32 (2005) 565–572.

[17] S.W. Sharshir, G. Peng, L. Wu, F.A. Essa, A.E. Kabeel, N. Yang, The effects of flake graphite nanoparticles, phase change material, and film cooling on the solar still performance, Appl. Energy 191 (2017) 358–366.

[18] Y.A.F. El-Samadony, A.E. Kabeel, Theoretical estimation of the optimum glass cover water film cooling parameters combinations of a stepped solar still, Energy 68 (2014) 744–750.

[19] K. Kalidasa Murugavel, K. Srithar, Performance study on basin type double slope solar still with different wick materials and minimum mass of water, Renew. Energy 36 (2011) 612–620.

[20] Z.M. Omara, A.E. Kabeel, F.A. Essa, Effect of using nanofluids and providing vacuum on the yield of corrugated wick solar still, Energy Convers. Manage. 103 (2015) 965–972.

[21] S.W. Sharshir, et al., Enhancing the solar still performance using nanofluids and glass cover cooling: Experimental study, Appl. Therm. Eng. 113 (2017) 684–693.

[22] K. Bae, G. Kang, S.K. Cho, W. Park, K. Kim, W.J. Padilla, Flexible thin-film black gold membranes with ultrabroadband plasmonic nanofocusing for efficient solar vapour generation, Nat. Commun. 6 (2015) 10103.

[23] H. Ghasemi, et al., Solar steam generation by heat localization, Nat. Commun. 5 (2014) 4449.

[24] X. Li, et al., Graphene oxide-based efficient and scalable solar desalination under one sun with a confined 2D water path, Proc. Natl. Acad. Sci. USA 113 (2016) 13953–13958.

[25] Y. Ito, Y. Tanabe, J. Han, T. Fujita, K. Tanigaki, M. Chen, Multifunctional porous graphene for high-efficiency steam generation by heat localization, Adv. Mater. 27 (2015) 4302–4307.

[26] Q. Jiang, et al., Bilayered biofoam for highly efficient solar steam generation, Adv. Mater. 28 (2016) 9400–9407.

[27] G. Ni, et al., Steam generation under one sun enabled by a floating structure with thermal concentration, Nat. Energy 1 (2016) 16126.

[28] L. Tian, et al., Plasmonic biofoam: A versatile optically active material, Nano Lett. 16 (2016) 609–616.

[29] L. Zhou, et al., 3D self-assembly of aluminium nanoparticles for plasmon-enhanced solar desalination, Nat. Photonics 10 (2016) 393–398.

[30] J.L. Plawsky, et al., Nano- and microstructures for thin-film evaporation—a review, Nanosc. Microsc. Therm. 18 (2014) 251–269.

[31] F. Su, H. Ma, X. Han, H.H. Chen, B. Tian, Ultra-high cooling rate utilizing thin film evaporation, Appl. Phys. Lett. 101 (2012) 113702.

[32] M. Ojha, A. Chatterjee, G. Dalakos, P.C. Wayner, J.L. Plawsky, Role of solid surface structure on evaporative phase change from a completely wetting corner meniscus, Phys. Fluids 22 (2010) 052101.

[33] K. Sefiane, On the role of structural disjoining pressure and contact line pinning in critical heat flux enhancement during boiling of nanofluids, Appl. Phys. Lett. 89 (2006) 044106.

[34] L.E. Helseth, T.M. Fischer, Particle interactions near the contact line in liquid drops, Phys. Rev. E 68 (2003) 042601.

[35] J. Yang, et al., Functionalized graphene enables highly efficient solar thermal steam generation, ACS Nano 11 (2017) 5510–5518.

[36] A. Kozbial, Z. Li, J. Sun, X. Gong, F. Zhou, Y. Wang, H. Xu, H. Liu, L. Li, Understanding the intrinsic water wettability of graphite, Carbon 74 (2014) 218–225.

[37] A. Kozbial, C. Trouba, H. Liu, L. Li, Characterization of the intrinsic water wettability of graphite using contact angle measurements: effect of defects on static and dynamic contact angles, Langmuir 33 (2017) 959–967.

[38] Z. Song, F. Guo, Y. Liu, S. Hu, X. Liu, Y. Wang, Controllable bidirectional wettability transition of impregnated graphite by laser treatment and transition mechanism analysis, Surf. Coat. Tech. 317 (2017) 95–102.

[39] G. Ni, et al., Volumetric solar heating of nanofluids for direct vapor generation, Nano Energy 17 (2015) 290–301.

[40] A.A. Balandin, Thermal properties of graphene and nanostructured carbon materials, Nat. Mater. 10 (2011) 569–581.

[41] Kunli Goh, et al., Carbon nanomaterials for advancing separation membranes: A strategic perspective, Carbon 109 (2016) 694–710.

[42] H. Malekpour, et al., Thermal conductivity of graphene with defects induced by electron beam irradiation, Nanoscale 8 (2016) 14608–14616.

[43] D.L. Nika, A.A. Balandin, Phonons and thermal transport in graphene and graphene-based materials, Rep. Prog. Phys. 80 (2017) 036502.

[44] H. Wang, S.V. Garimella, J.Y. Murthy, Characteristics of an evaporating thin film in a microchannel, Int. J. Heat Mass Tran. 50 (2007) 3933–3942.

[45] R. Caringella, et al., Electrically conducting linen fabrics for technical applications, Text. Res. J. 004051751667606 (2016).

[46] C.-I. Su, J.-X. Fang, X.-H. Chen, W.-Y. Wu, Moisture absorption and release of profiled polyester and cotton composite knitted fabrics, Text. Res. J. 77 (2007) 764–769.

[47] J.F. Davies, R.E. Miles, A.E. Haddrell, J.P. Reid, Influence of organic films on the evaporation and condensation of water in aerosol, Proc. Natl. Acad. Sci. U.S.A. 110 (2013) 8807–8812.

[48] S. Moosman, G. Homsy, Evaporating menisci of wetting fluids, J. Colloid Interf. Sci. 73 (1980) 212–223.

[49] J.B. Freund, The atomic detail of an evaporating meniscus, Phys. Fluids 17 (2005) 022104.

[50] E.M. Hotze, T. Phenrat, G.V. Lowry, Nanoparticle aggregation: challenges to understanding transport and reactivity in the environment, J. Environ. Qual. 39 (2010) 1909.

[51] Y.T. He, J. Wan, T. Tokunaga, Kinetic stability of hematite nanoparticles: the effect of particle sizes, J. Nanopart. Res. 10 (2007) 321–332.

[52] R. Ranjan, J.Y. Murthy, S.V. Garimella, A microscale model for thin-film evaporation in capillary wick structures, Int. J. Heat. Mass. Tran. 54 (2011) 169–179.

[53] S. Giordani, et al., Debundling of single-walled nanotubes by dilution: observation of large populations of individual nanotubes in amide solvent dispersions, J. Phys. Chem. B 110 (2006) 15708–15718.

Supplemental Information

Low-cost high-efficiency solar steam generator by combining thin film evaporation and heat localization: both experimental and theoretical study

Guilong Peng[1,2,#], Hongru Ding[1,2,#], S.W. Sharshir[1,2,3], Xiaojia Li[1,2], Hanchen Liu[1,2], Dengke Ma[1,2], Lirong Wu[1,2], Jianfeng Zang[4,5], Huan Liu[4], Wei Yu[6], Huaqing Xie[6], Nuo Yang[1,2,*]

1 State Key Laboratory of Coal Combustion, Huazhong University of Science and Technology, Wuhan 430074, China

2 Nano Interface Center for Energy (NICE), School of Energy and Power Engineering, Huazhong University of Science and Technology, Wuhan 430074, China

3 Mechanical Engineering Department, Faculty of Engineering, Kafrelsheikh University, Kafrelsheikh, Egypt.

4 School of Optical and Electronic Information, Huazhong University of Science and Technology, Wuhan 430074, China

5 Innovation Institute Huazhong University of Science and Technology, Wuhan 430074, China

6 School of Environment and Materials Engineering, College of Engineering, Shanghai Second Polytechnic University, Shanghai 201209, China

[#]Guilong Peng and Hongru Ding contribute equally on this work.

*Corresponding email: nuo@hust.edu.cn

I Measurement setup

The setup is shown in Fig S1. A solar simulator (CEL-S500, AM1.5 filter) was used to generate the solar beam, the solar intensity was measured by a power meter (PM-150-50C) and adjusted to 1kw/m^2. During the experiment, the edge of wick layer and the bulk water were insulated by polyurethane foam (PU, 2.5cm thick) to minimize the heat loss. The diameter of the evaporation layer is 5 cm, to cut the solar beam to the same diameter, a beam shelter slice was placed between the solar output window and the evaporation layer. The mass change during the evaporation process was measured by an electric balance (Sartorius Practum 224), the data were recorded by a computer via a USB cable. The room temperature and humidity during the experiment were controlled at 24 ℃ and 40% respectively. The temperature was measured by T type thermal couple (Omega, TT-T-40-SLE), and a data acquisition device (Keithley 2700) were used to record the temperature.

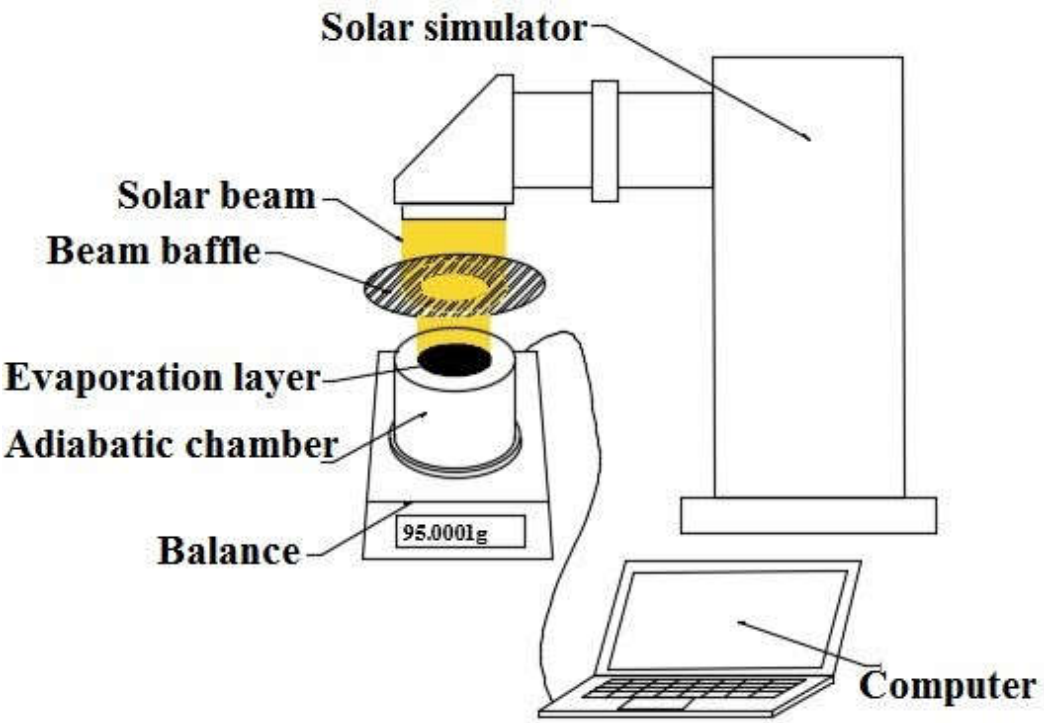

Fig. S1. The schematic diagram of measurement setup.

II Recycle of particles

The graphite particles we used have large lateral size, which makes they much easier to be recycled. Figure S2 shows the recycle process qualitatively, Figure S2a shows a piece of linen coated by graphite particles (1.3μm), here the linen is white for a better presentation. Then the contaminated linen was washed by clean water without using detergent as shown in Figure S2b. The washed linen can be as clean as Figure S2c shows. Only a few of particles are adhere to the linen. At first the particles will suspend in the wash water, but due to the aggregation, most of the particles will deposit, and some of them will float on the water surface due to the surface tension as shown in Figure S2d. The deposited and floated particles form large size particle clusters which make sure the new linen cloth can retain them, instead of penetrating the cloth as shown in Figure S2e. Consequently, the filtered water is quite clean as shown in Figure S2f.

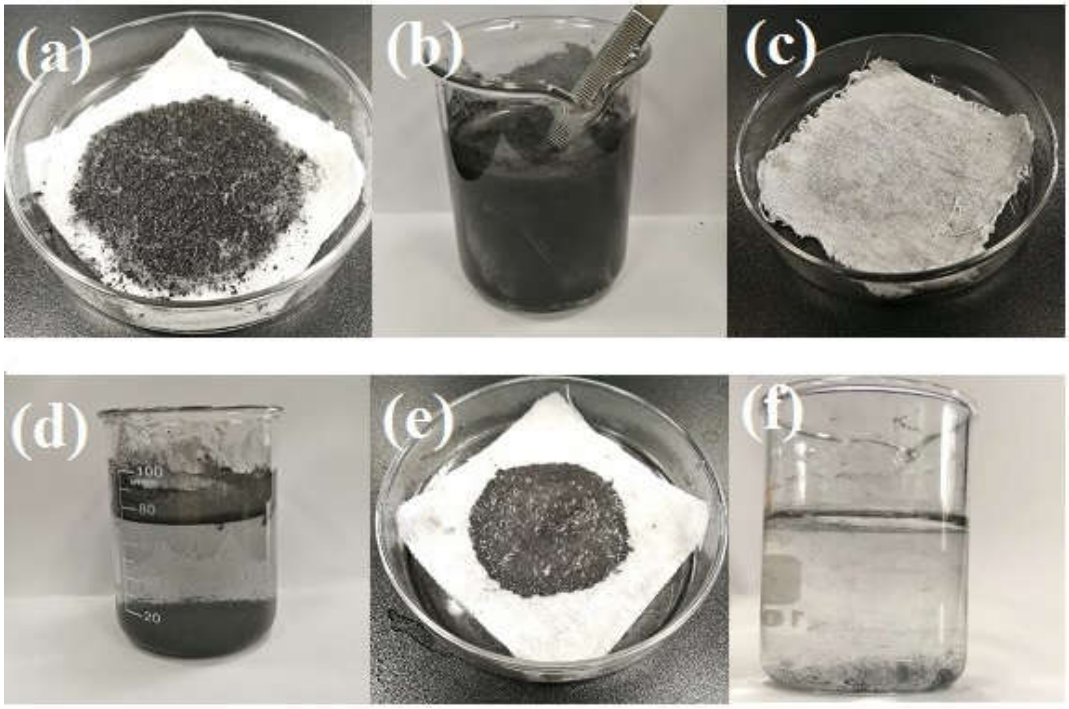

Fig. S2 a) The white linen coated by graphite particles (1.3μm), b) Washing linen by water, the particles will fall off. c) The washed linen, only a few particles are still on it. d) Graphite particles aggregate and deposit after washing. e) The aggregated particles can be collected by filtering with new linen cloth. f) the filtered water is quite clean, indicates a good recycle effect.

III Images and parameters of materials

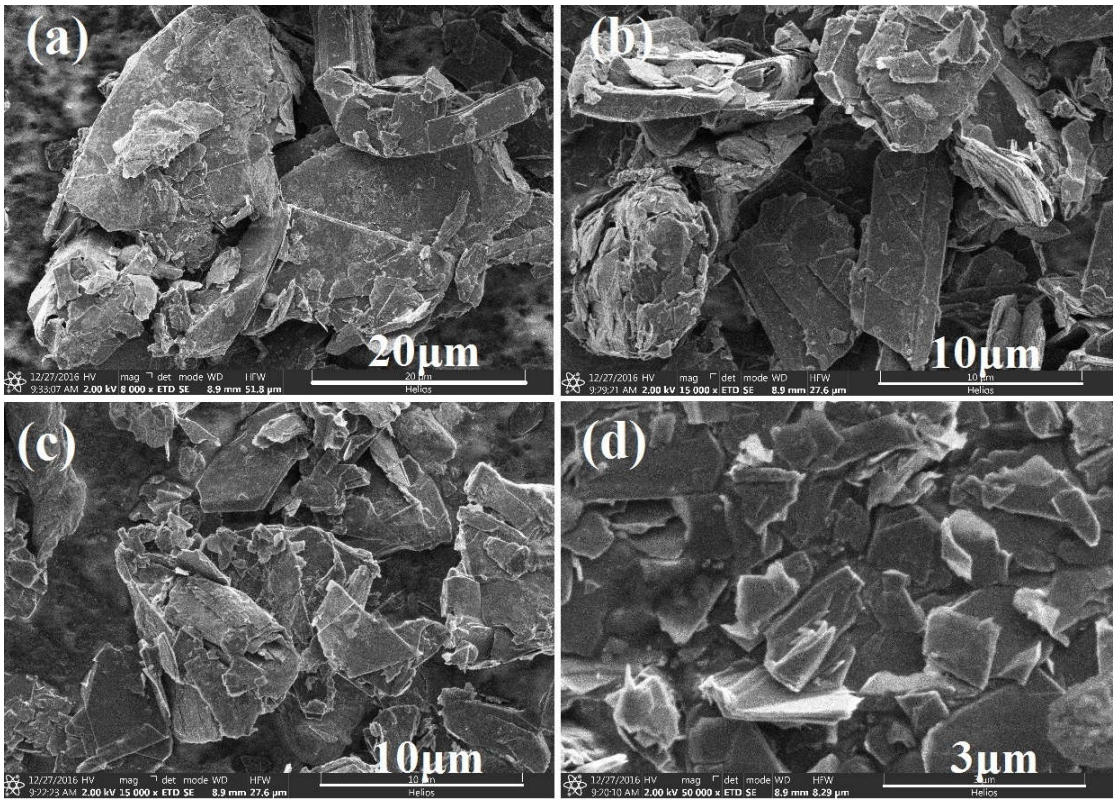

Fig. S3 The SEM image of the four different sizes graphite particles: separated by 500 mesh (~25μm hole size), 1000 mesh (~13μm hole size), 2000 mesh (~6.5μm hole size), and 10000 mesh (~1.3μm hole size) sieves. a) 500mesh graphite particles, b) 1000mesh graphite particles, c) 2000mesh graphite particles, d) 10000mesh graphite particles.

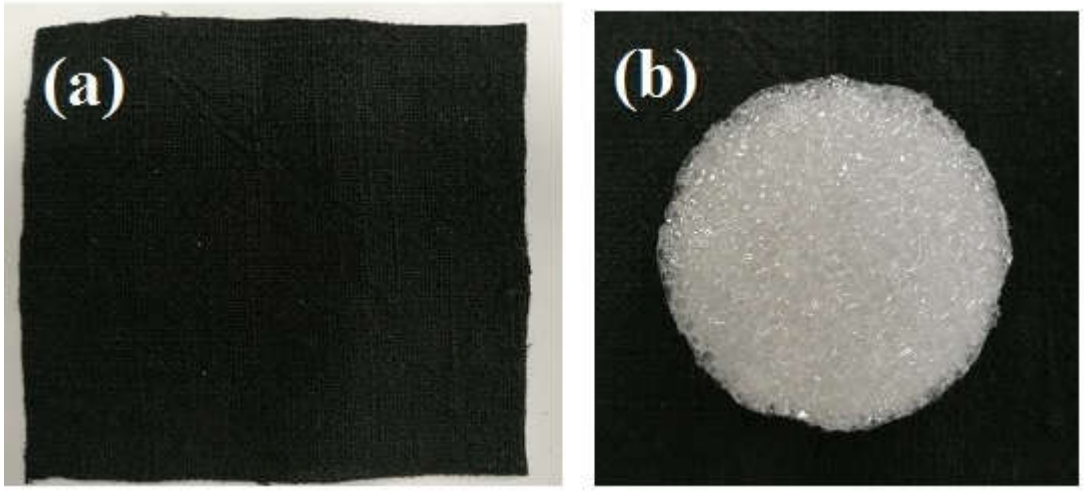

Fig. S4 a) The picture of linen cloth. b) The picture of the EPE foam.

Table S1 The characteristics of the linen and EPE used in experiment.

material	characteristic	value
linen	Rate of moisture regain, (%)	12.5
	Mass density, (g/m^2)	250
	Thickness, (mm)	1
	Thermal conductivity, (W/(m·K))	0.03-0.04
EPE	Mass density, (g/cm^3)	0.03
	Thickness, (cm)	1
Graphite	Purity, (%)	>99.9%

IV Absorptivity of different cases

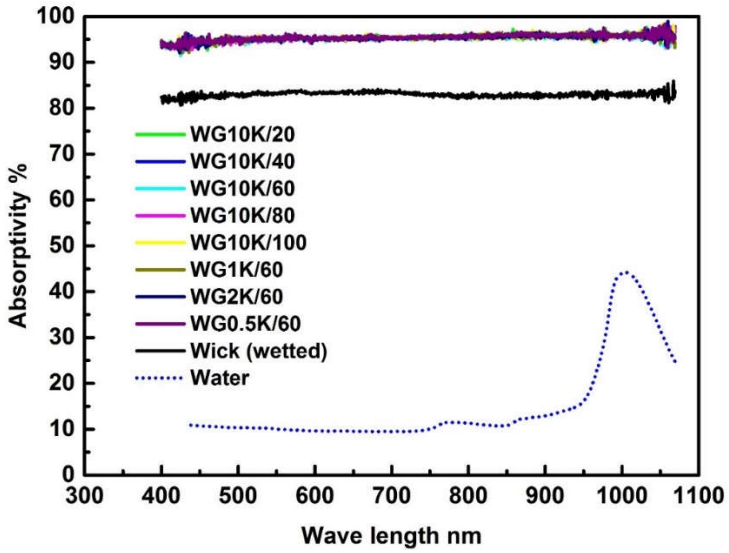

Fig. S5 The absorptivity of different material. 0.5K, 1K, 2K and 10K are 500, 1000, 2000 and 10000mesh, respectively. 20, 40, 60, 80, 100, 180 indicate the concentrations, the unit is g/m^2.

V Effect of salt on evaporation

To show the potential of using our generator in desalination, we measured the mass reduction of salt water (3.5% wt. of salt, which is the same salt concentration as sea water). As shown in Fig. S6, salt has negligible effect on the evaporation rate compared with tap water, due to the salt-rejecting ability of wick type solar steam generator. A similar results was also found by Ni et al.[1]. Therefore, our wick type steam generator is a good candidate for desalination system.

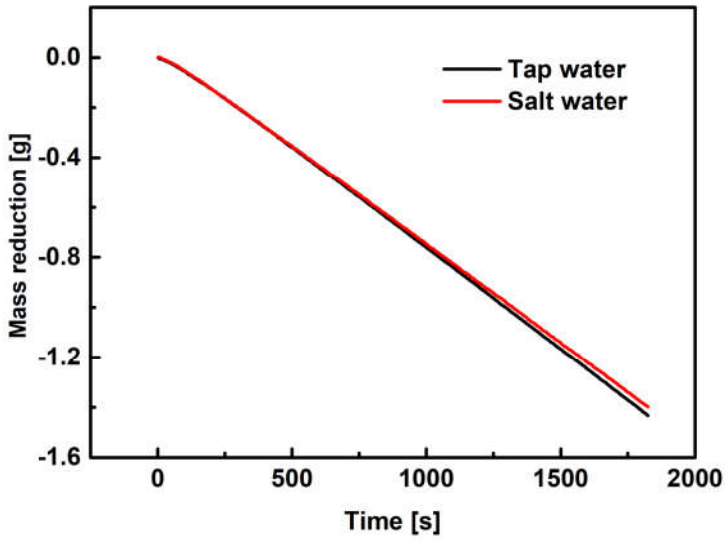

Fig. S6 The evaporation rate of salt water (3.5% wt.) and tap water.

VI Thin-film evaporation

(i) Thin-film region area for different particle size

The shape of graphite micro/nanoparticle is assumed to be a cylinder with diameter d and height h, as shown in Fig. S7. In addition, the size of each particle is also assumed to be same. The gross mass of graphite particles, M, is given by,

$$M = NV\rho = \frac{Nh\rho\pi d^2}{4} \quad \text{(S1)}$$

where N is the number of graphite particles; ρ is the density of graphite particles. If we ignore the aggregation of graphite, the gross lateral area of graphite cylinders can be defined as,

$$S_l = N\pi dh \quad \text{(S2)}$$

Eq. (S1) is substituted into Eq. (S2),

$$S_l = \frac{4M}{\rho d} \tag{S3}$$

For a given mass concentration, M is the same in all cases. And the area of thin-film region, A is proportional to the contact areas where liquid, vapor and solid meet, i.e. the lateral areas of graphite cylinder, S_l. That is,

$$A \propto \frac{l}{d} \tag{S4}$$

If the aggregation is considered, the lateral areas of graphite cylinder S_l is inversely proportional to the probability, multiplying by the probability that two graphite particles attach, which is sticking coefficient, also known as the attachment efficiency α [2]. Then,

$$A \propto \frac{1}{\alpha(d)d} \tag{S5}$$

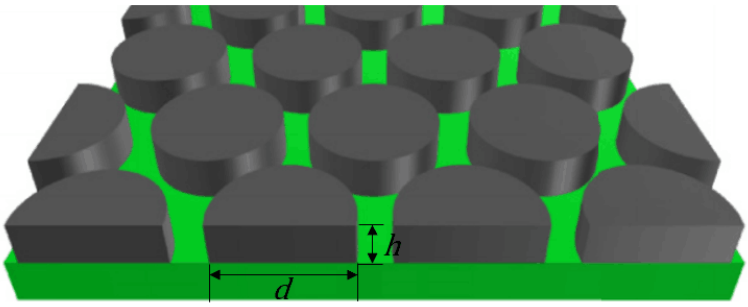

Fig. **S7** Ideal uniform distribution of the particles on the water surface

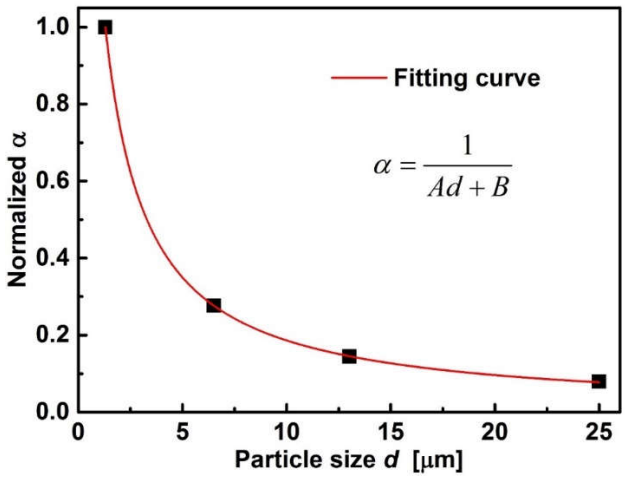

Fig. S8 The normalized sticking coefficient versus graphite particle size. A and B are the fitting coefficient.

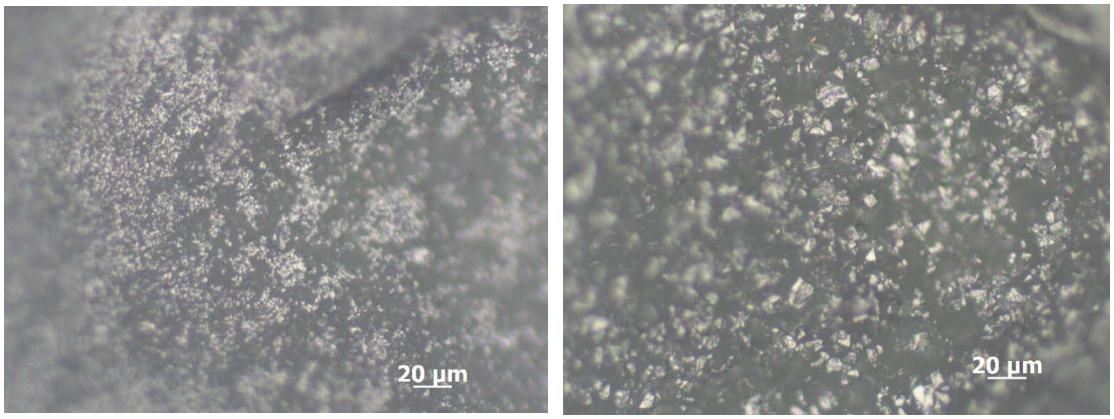

(a) (b)

Fig. S9 a) The 10000 mesh particles on water, the particles intend to aggregate to larger size, which makes the contact area between water and particles decreases a lot. b) The 1000 mesh particles on water, the particles disperse more uniformly.

(ii) Thin-film thickness for different particle size

The thickness of thin film varies with different particle size and is calculated based on the data of Wang et.al [3]. The adsorbed thin film thickness, δ_0, (i.e. the thickness of region I in manuscript Fig. 2d) is given by [4],

$$\delta_0 = \left(\frac{A_h V_l T_v}{M h_{lv}(T_{lv}-T_v)}\right)^{1/3} \quad \text{(S6)}$$

where V_l is the molar volume; T_v is the temperature of vapor; M is molecular weight; h_{lv} is the enthalpy of vaporization; T_{lv} is the temperature of solid-liquid interface; A_h is Hamaker constant [5],

$$A_h = \pi^2 C \rho_1 \rho_2 \quad \text{(S7)}$$

where ρ_1 and ρ_2 are the number densities of graphite and water, and C is the coefficient in the particle–particle pair interaction.

We substitute the parameters, including molecular weight, density and so on, of water into those of the liquid (octane) in ref. S4 and get the adsorbed thin film thickness, δ_0, of this work. Then we get the ratio of thin film thickness in this work to that of ref. S4. Then $\delta(d)$ is calculated according to the ratio and the thin film thickness of octane.

It should be noted, to simplify the calculation, $\delta(d)$ equals to the average value of thin film thickness.

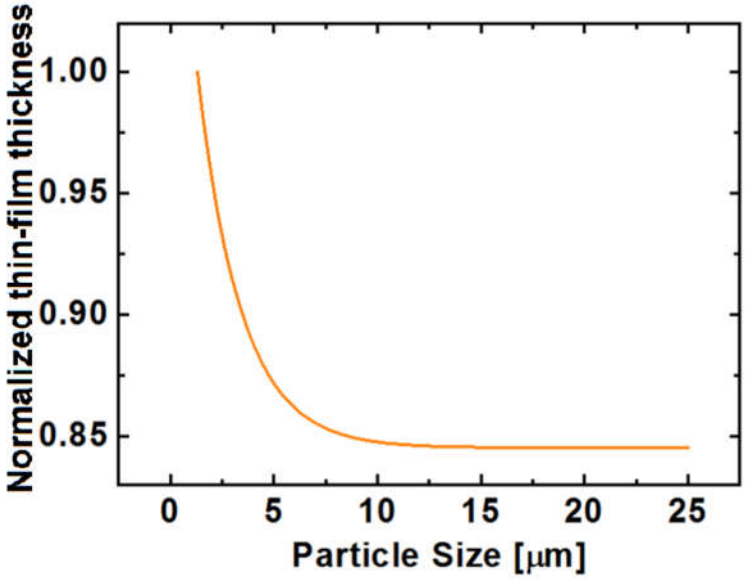

Fig. S10 Normalized average thin-film thickness of different particle size

As shown in fig. S10, $\delta(d)$ decreases with the growing particle size. The variation of disjoining pressure and capillary pressure along the meniscus provide the necessary pressure gradient for liquid supply in the thin-film region and decide the shape of meniscus [6]. The location where the disjoining pressure drops to 1/5000th of the initial value marks the end of thin-film region. The drop of capillary pressure decides the curvature of the thin film profile. Bigger particles possess bigger channels hence sharper drops [4], which flattening the thickness profile more drastically. Therefore, $\delta(d)$ reduces with growing d.

VII Definition of stable state

In this work, the stable state means the state when evaporation rate and energy efficiency almost do not change with time. We calculated the slope of the curves in Fig. 2a for every 400s, which shows the evaporation rate. As shown in Fig. S11, the stable state is reached after around 800s for W&E&G and W&E. Therefore, the hourly evaporation rate is the evaporation rate after 800s.

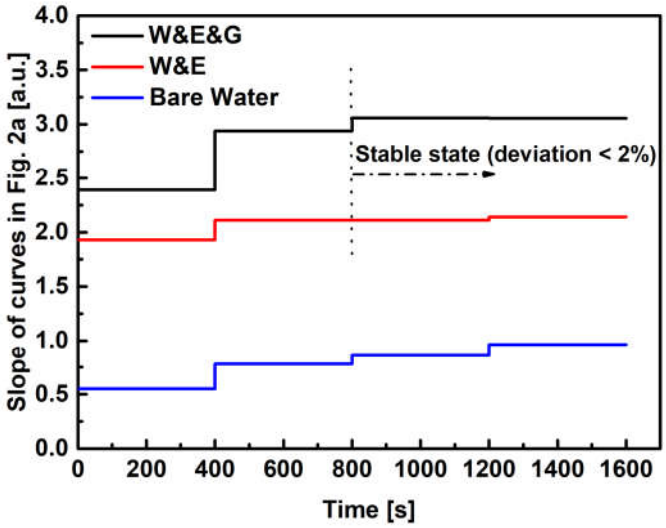

Fig. S11 The slope of the curves in Fig. 2a for every 400s.

References :

[1] Ni G, Zandavi SH, Javid SM, Boriskina SV, Cooper TA, Chen G. A salt-rejecting floating solar still for low-cost desalination. Energy & Environmental Science 11, 1510-1519 (2018).

[2] Hotze EM, Phenrat T, Lowry GV. Nanoparticle Aggregation: Challenges to Understanding Transport and Reactivity in the Environment. *J. Environ. Qual.* **39**, 1909 (2010).

[3] Wang H, Garimella SV, Murthy JY. Characteristics of an evaporating thin film in a microchannel. Int. J. Heat Mass Tran. 50, 3933-3942 (2007).

[4] Wayner PC, Kao YK, LaCroix LV. The interline heat-transfer coefficient of an evaporating wetting film. *Int J Heat Mass Tran* **19**, 487-492 (1976).

[5] Hamaker HC. The London—van der Waals attraction between spherical particles. *Physica* **4**, 1058-1072 (1937).

[6] Potash M, Wayner PC. Evaporation from a two-dimensional extended meniscus. *Int J Heat Mass Tran* **15**, 1851-1863 (1972).